Review
Article

phys. stat. sol. (b) **242**, No. 1, 11–29 (2005) / **DOI** 10.1002/pssb.200404959

Review Article

A review of electron–phonon coupling seen in the high-T_c superconductors by angle-resolved photoemission studies (ARPES)

T. Cuk[*, 1], **D. H. Lu**[1], **X. J. Zhou**[1], **Z.-X. Shen**[1], **T. P. Devereaux**[2], and **N. Nagaosa**[3]

[1] Departments of Physics, Applied Physics and Stanford Synchrotron Radiation Laboratory, Stanford University, Stanford, CA 94305, USA
[2] Department of Physics, University of Waterloo, Waterloo, Ontario N2L 3G1, Canada
[3] CREST, Department of Applied Physics, University of Tokyo, Bunkyo-ku, Tokyo 113, Japan

Received 30 September 2004, revised 13 November 2004, accepted 15 November 2004
Published online 10 December 2004

PACS 71.38.–k, 72.10.–d, 74.25.Jb, 74.25.Kc, 74.72.Hs, 79.60.–i

We review recent experimental results and phenomenological models of the electron–phonon interaction in high-T_c superconductors as seen by angle-resolved photoemission (ARPES). We focus on the relatively higher doped systems for which the data is reminiscent of a single phonon process and highlight evidence for the relevance of several specific phonon modes to these materials.

Contents

1 Introduction

2 Background on the spectral function seen by ARPES
2.1 Theoretical representation of the spectral function and electron–phonon self energies
2.2 Experimental signatures of electron–phonon coupling

3 Early results on the mode-coupling in the cuprates

4 Recent results on the mode-coupling in the cuprates
4.1 Half-breathing phonon mode and the spin resonance mode
4.2 The B_{1g} bond-buckling phonon mode
4.3 The maximum entropy method
4.4 Isotope effects in ARPES

5 Conclusion

References

[*] Corresponding author: e-mail: tanjacuk@stanford.edu

1 Introduction

The physical mechanism underlying pairing in high temperature superconductors is far from being understood. While initially the very nature of d-wave pairing suggested the importance of a spin-based pairing interaction, there has been a recent accumulation of experimental results suggesting that the electron–phonon interaction must play an important role in these materials. This evidence has come from Raman spectroscopy, neutron scattering, and penetration depth measurements, but a large body of experimental results from angle resolved photoemission (ARPES) have suggested that several specific phonon modes may be of relevance.

The purpose of this mini-review is to pedagogically go through the most prominent and researched ARPES data on electron-phonon coupling in the high-T_c cuprates. In so doing, we will highlight evidence for prominent energy scales in the high-T_c problem, review past and present attempts to interpret those energy scales, and introduce recent phenomenological models to characterize the momentum and temperature dependence of the mode coupling behavior. We divide the review into three sections: (i) background on the spectral function seen by ARPES, (ii) early, and (iii) recent results on the mode-coupling in the cuprates. We focus our effort on the behavior seen in the ARPES data that is reminiscent of a single-phonon process and can describe relatively higher doped systems. Calculations in the context of conventional superconductivity [1–4] have been extended to the cuprate superconductors [5–9]. We do not go into aspects of the data that indicate polaronic behavior, involving multiple-phonon processes, that is more characteristic of the deeply under-doped regime of some systems [10, 11].

2 Background on the spectral function seen by ARPES

2.1 Theoretical representation of the spectral function and electron–phonon self energies

Physical observables are represented by the correlation functions of operators that describe the particles involved in the physical process [12]. For example, the conductivity is given by the current–current correlation function, where the current is written as the product of the creation and annihilation operators of electrons. Most physical observables are given by the two-particle correlation (Green's) functions, and their connection to the single-particle spectral function is indirect and requires theoretical assumptions. In this respect, angle-resolved photoemission spectroscopy (ARPES) is a unique and powerful tool providing direct information on the single-particle spectral function of electrons. In the context of the "sudden approximation" described below, the single particle spectral function measured by ARPES can be written in the following way:

$$A(k,\omega) = -(1/\pi)\,\mathrm{Im}\,G(k,\omega)\,, \tag{1}$$

$$G(k,\omega) = \frac{Z(k,\omega)\,\omega + \varepsilon(k) + \chi(k,\omega)}{(Z(k,\omega)\,\omega)^2 - (\varepsilon(k) + \chi(k,\omega))^2 - \phi(k,\omega)^2}\,, \tag{2}$$

where Z, χ, and ϕ represent a renormalization due to either electron–electron or electron–phonon interactions and $\varepsilon(k)$ is the bare-band energy. In the weak coupling case, $Z = 1$, $\chi = 0$, and $\phi = \Delta$, the superconducting gap. The same formalism can be extended to the normal state by setting $\phi = 0$. In the normal state, the spectral function can be written in a more compact way, in terms of the real and imaginary parts of the self energy that determine Z, χ, and ϕ:

$$A(k,\omega) = \frac{-\mathrm{Im}\,\Sigma(k,\omega)/\pi}{(\omega - \varepsilon(k) - \mathrm{Re}\,\Sigma(k,\omega))^2 + (\mathrm{Im}\,\Sigma(k,\omega))^2}\,. \tag{3}$$

Writing down this $A(k,\omega)$ for the photoemission experiment is based on the sudden approximation as discussed in detail elsewhere [13]. Here we cite the prominent assumptions:

(1) The excited state of the sample (created by the ejection of the photo-electron) does not relax in the time it takes for the photo-electron to reach the detector. The so-called "udden-approximation" allows one to write the final state wave-function in a separable form, $\Psi_f^N = \Phi_f^k \Psi_f^{N-1}$, where Φ_f^k denotes the photoelectron and Ψ_f^{N-1} denotes the final state of the bulk material with $N-1$ electrons. If the system is non-interacting, then the final state overlaps with a single eigenstate of the Hamiltonian describing the $N-1$ electrons. In the interacting case, the final state can overlap with all possible eigenstates of the $N-1$ system.

(2) In the interacting case, this $A(k, \omega)$ describes a "quasiparticle" picture in which the interactions of the electrons with lattice motions as well as other electrons can be treated as a perturbation to the bare band dispersion, $\varepsilon(k)$, in the form of a self energy, $\Sigma(k, \omega)$. The validity of this picture as well as (1) rests on whether or not the spectra can be understood in terms of well-defined peaks representing poles in the spectral function.

This $A(k, \omega)$ does not incorporate the following, which also contribute to the intensity of real spectra and are nicely described by the three-step description of photoemission [14]:

(3) Electrons scattered inelastically by the photo-electron before it exits the sample, which contribute a background (though relatively smooth) to the spectra.

(4) The matrix element representing the transition of the incoming photon to the outgoing photoelectron could in general depend on the initial electron momentum, k, the incident photon energy, $\hbar\nu$, the polarization of the light with respect to the sample, as well as the final state configuration.

(5) The surface is treated no differently than the bulk in this $A(k, \omega)$. In reality surface states are expected and are observed and can lead to confusion in the data interpretation [15].

Even with these considerations, the spectral function remains a good starting point for describing dynamics seen in the spectra due to coupling of the electrons to sharp phononic modes. In fact for conditions in which the peak width in the spectra close to the Fermi level is fairly narrow (20–30 meV), dominant features of the mode coupling behavior can be captured using the following form for the self-energy:

$$\Sigma(k, \omega) = \sum_{q,\nu} g^2(k, q)\, D(q, \nu)\, G(k - q, \omega - \nu)\,, \tag{4}$$

where $D(q, \omega) = \dfrac{2\Omega_q}{\omega^2 - \Omega_q^2}$ is the phonon propogator and Ω_q is the phonon energy.

In this form of the self energy, corrections to the electron–phonon vertex, g, are neglected. Migdal's Theorem states that corrections to the vertex are of order $\lambda\Omega/E_f$ [16]. While for most metals, this quantity is negligible, in the case of the cuprates, these corrections may become appreciable. Nevertheless, a phenomenological treatment using this self-energy reproduces the dominant features of the data well for optimally and over-doped samples. For most of this review, furthermore, we assume only one-iteration of the coupled self-energy and green's function equations. In other words, in the equation for the self energy, Σ, we assume bare electron and phonon propagators, G_0 and D_0 respectively, which both simplifies the calculations and allows us to see how much of the dynamics we can capture with just the leading order term. With these assumptions, the imaginary parts of the functions Z, χ, and ϕ, denoted as Z_2, χ_2, and ϕ_2, in the full temperature dependent form are:

$$\begin{aligned} Z_2(k, \omega)\,\omega = \sum_q g^2(k, q)\,(\pi/2)\,(\delta(\omega - \Omega_q - E_{k-q}) + \delta(\omega - \Omega_q + E_{k-q}))\,(f(\Omega_q - \omega) + n(\Omega_q)) \\ + (\delta(\omega + \Omega_q - E_{k-q}) + \delta(\omega + \Omega_q + E_{k-q}))\,(f(\Omega_q + \omega) + n(\Omega_q))\,, \end{aligned} \tag{5}$$

$$\begin{aligned} \chi_2(k, \omega) = \sum_q - g^2(k, q)\,(\pi\varepsilon_{k-q}/2E_{k-q})\,(\delta(\omega - \Omega_q - E_{k-q}) \\ - \delta(\omega - \Omega_q + E_{k-q}))\,(f(\Omega_q - \omega) + n(\Omega_q)) \\ + (\delta(\omega + \Omega_q - E_{k-q}) - \delta(\omega + \Omega_q + E_{k-q}))\,(f(\Omega_q + \omega) + n(\Omega_q))\,, \end{aligned} \tag{6}$$

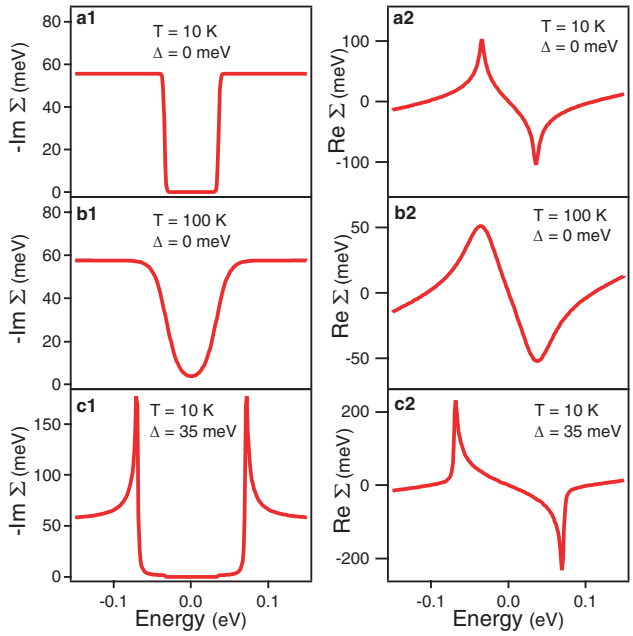

Fig. 1 Self energy for electrons coupling to an Einstein mode with Ω = 35 meV and electron-phonon vertex $g = 0.15$ eV. (a1), (b1), and (c1) plots Im $\Sigma = -Z_2\omega + \chi_2$ for a normal state electron at 10 K, for a normal state electron at 100 K, and for an electron in an s-wave superconducting state at 10 K, respectively. (a2), (b2), and (c2) plots the corresponding real parts, Re Σ, obtained using the Kramers–Kronig relation.

$$\phi_2(k,\omega) = \sum_q g^2(k,q)\,(\pi\Delta_{k-q}/2E_{k-q})\,(\delta(\omega-\Omega_q-E_{k-q}) - \delta(\omega-\Omega_q+E_{k-q}))\,(f(\Omega_q-\omega)+n(\Omega_q))$$

$$+\,(\delta(\omega+\Omega_q-E_{k-q}) - \delta(\omega+\Omega_q+E_{k-q}))\,(f(\Omega_q+\omega)+n(\Omega_q))\,, \qquad (7)$$

where $f(x)$, $n(x)$ are the Fermi, Bose distribution functions and E_k is the superconducting state dispersion, $E_k^2 = \varepsilon_k^2 + \phi_k^2$.

The above equations are essentially those of Eliashberg theory for strongly-coupled superconductors (although λ can be large (>1), i.e., "strongly-coupled", still vertex corrections and multi-phonon processes are negligible due to the Fermi degeneracy and small Ω/E_F) [1]. Figure 1 plots $-Z_2\omega + \chi_2$, the imaginary part of the phonon self-energy, Im Σ, that represents the renormalization to the diagonal channel of the electron propagator, or the one in which the charge number density is subjected to electron–phonon interactions. This part of the self-energy gives a finite lifetime to the electron, and consequently broadens the peak in the spectra (Im Σ in $A(k,\omega)$ (Eq. (3)) is the HWHM of the peak). Figure 1 shows several illustrative cases of what the electron–phonon interaction can do to the electron's lifetime using an Einstein phonon and constant, isotropic g coupled to a parabolic electronic band. We present this calculation in the spirit of Engelsberg and Schrieffer, who first calculated the spectral function for an electron–phonon coupled system [17] and which later provided the foundation for the later work by Scalapino, Schrieffer, and Wilkins [3] on the superconducting state. For the normal state electron at 10 K (Fig. 1(a1)), there is a sharp onset of the self energy that broadens the spectra beyond the mode energy; for the normal state electron at 100 K (Fig. 1(b1)), the onset of the self-energy is much smoother and occurs over ~50 meV; for the superconducting state electron (Fig. 1(c1)), there is a singularity that causes a much more abrupt broadening of the spectra at the energy $\Omega + \Delta$. The superconducting state singularity is due to the density of states pile up at the gap energy; the energy at which the decay onsets shifts by Δ, since below the gap energy there are no states to which a hole created by photoemission can decay. For each of these imaginary parts of the self energy, one can use the Kramers–Kronig transform to obtain the real part of the self energy, which renormalizes the peak position (Re Σ in $A(k,\omega)$ (Eq. (3)) changes the position of the peak in the spectral function). The real self energies thereby obtained are also plotted in Fig. 1(a2), Fig. 1(b2), and Fig. 1(c2). In the superconducting state, again there is a singularity that causes a more abrupt break from the bare-band dispersion at the energy $\Omega + \Delta$.

For most metals, where the electrons are weakly interacting, and therefore the poles of the spectral function are well-defined, one would expect such a treatment to hold and indeed it does, as evidenced by several cases including beryllium [18, 19] and molybdenum [20]. A priori, one might not expect the same to hold in ceramic materials such as the copper-oxides, where the copper d-wave electrons are localized and subject to strong electron–electron and electron–phonon interactions. Nonetheless, in the superconducting state of the copper-oxides, one recovers narrow peaks of the spectral function. The above self-energy, then, is able to describe the phenomenology of the mode-coupling behavior for the superconducting state of under-doped, optimally doped, and over-doped cuprates. It also captures the major changes in the spectra between the normal state and the superconducting state for the optimally and over-doped cuprates, although it fails to describe the detailed behavior of the normal state and the pseudo-gap. For the phenomenology of the under-doped cuprates where the electron-phonon and electron–electron interactions are thought to be considerably stronger, one needs to turn to the "polaronic" rather than "Fermi liquid" regime in which the electron is not freely moving but rather bound to a gas of phonons or other electronic modes. In this "polaronic" picture, the electron's velocity or band dispersion is treated as a perturbation to its interaction with lattice motions/electronic modes. We leave this discussion for continuing [10, 11] and future work.

2.2 Experimental signatures of electron–phonon coupling

In Fig. 2, we show the ARPES spectral function for a parabolic band coupled isotropically to an Einstein mode at 10 K in the normal state. The self energy included in this $A(k, \omega)$ is shown above in Fig. 1(a1)

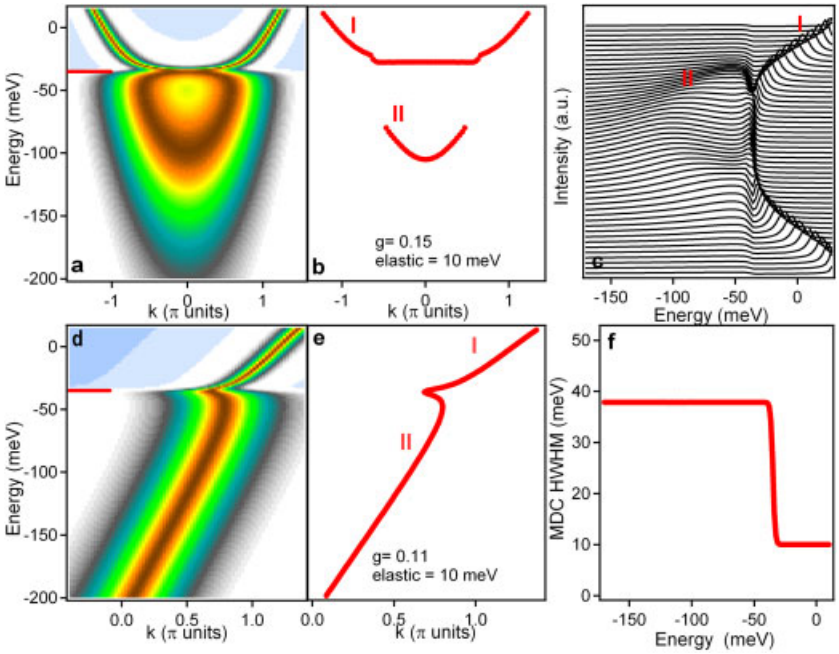

Fig. 2 (a) An image plot of the spectral function ($A(k, \omega)$) with a narrow, parabolic bare band dispersion (characterized by a band bottom ~ 120 meV) and the Im Σ and Re Σ shown in Fig. 1(a1) and Fig. 1(a2). (b) The EDC-derived dispersion for the spectral function shown in (a). (c) The EDCs of the spectral function shown in (a), where "I" indicates the "peaks" and "II" indicates the "humps". (d) An image plot of the spectral function ($A(k, \omega)$) with a linear bare-band dispersion and the Im Σ and Re Σ shown in Fig. 1(a1) and Fig. 1(a2), but using a slightly different magnitude for the vertex, g ($g = 0.11$ instead of $g = 0.15$). (e) The MDC-derived dispersion of the spectral function shown in (d). (f) The MDC-derived width of the spectral function shown in (e). Elastic self energies of 10 meV were also incorporated in the spectral functions to broaden the narrow poles and simulate better real spectra.

and Fig. 1(a2). Figures 2a and 2d show image plots of the spectral function one would expect in such a model for two different band dispersions. Figure 2c shows the Energy Distribution Curves (EDCs – spectral weight as a function of energy for each momentum slice). There are three characteristic signatures of mode coupling behavior evident in this model spectral function that show up in the data as well:

1) A break up of a single dispersing peak into two branches – a peak that decays as it asymptotically approaches the mode energy, and a hump that traces out a dispersing band. The peak that asymptotically approaches the mode energy derives from strong mixing of the electronic band with the mode, while the hump traces out the bare band dispersion away from the mode energy. In Fig. 2c (plot of the EDCs), the band dispersion clearly breaks up in two parts – the peaks are indicated by "I" and the humps by "II".

2) In the image plots, a significant broadening of the spectra beyond the mode energy is readily apparent. This is also the origin of the broad hump of the dispersing band seen in the EDCs (Fig. 2c). Such broadening of the spectral weight is due to the sharp onset of the self-energy seen in Fig. 1(a1) at the mode energy. Beyond the mode energy, the hole created in the photoemission process decays into a hole and a phonon, causing the lifetime of the measured photo-electron to shorten and the spectra to broaden.

3) At the mode energy itself, there is a "dip" between the peak and the hump in the EDCs (Fig. 2c) leading to the "peak-dip-hump" structure often discussed in the literature. The effect can also be readily seen in the image plots as a depletion of spectral weight at the mode energy, especially in the case of more strongly coupled bands than shown here but appropriate for the cuprates (see anti-nodal data shown in Fig. 7). When the electronic states and the mode coincide in energy, a hole can decay into a phonon and a hole sitting at the Fermi level (or in the case of the superconducting state, at the gap energy). This process has a higher probability of occurring than any other since the excited hole can be replaced by an electron sitting at the Fermi level for which holes and electrons have equal occupation numbers.

We now analyze this simulated data by tracking the peak/hump positions and widths of the resulting $A(k, \omega)$. In Fig. 2b, we track the peak and the hump positions of the spectral function shown in Fig. 2a and Fig. 2c. One could also find the peak positions by fitting the Momentum Distribution Curves (MDC, spectral weight as a function of momentum) to Lorentzians. In Fig. 2e, we show the results of such a fit for the spectral function shown in Fig. 2d. The top portion of this dispersion corresponds to the "peaks" and the bottom to the "humps" as indicated. The lorentzian fits will also give the widths of the peaks as a function of momentum. Those widths are plotted in Fig. 2f and exhibit an onset of spectral broadening/decrease in lifetime at the mode energy. The reason that one can use Lorentzians to fit the MDC spectra but not the EDC spectra, is because the self-energy depends less on the momentum than on the energy. In the case that the bare band dispersion is linear in k (the case for the spectral function shown in Fig. 2d), and the self-energy is independent of k (true for an Einstein phonon and isotropic vertex g), the width recovered from a Lorentzian fit would then be exactly the imaginary part of the self energy. Therefore, the MDC width recovered in Fig. 2e has the same form as the $\mathrm{Im}\,\Sigma$ shown in Fig. 1(a1) (the quantitative differences are due to an elastic self energy added to simulate real spectra ($\sim$10 meV) and a somewhat different g). Please see LaShell et al. for a more detailed look at the MDC-method [21]. For narrow bands (true for the cuprates, and many other materials) such as that shown in Fig. 2a, the bare band dispersion near the Fermi level is far from linear, making the spectral weight as a function of momentum deviate substantially from a Lorentzian. For most directions in the Brillouin zone of the cuprates (with the important exception of the nodal direction and near it), it is more appropriate to fit the EDCs phenomenologically to get peak/hump positions and widths, where the assumption of a linear bare band is not needed. There is then, however, no easy way of de-convolving the self-energies directly from the spectra. Instead, a calculated spectral function from an assumed self-energy can be compared directly with experimental spectra to obtain important parameters.

From these types of analysis, one could try and ascertain the mode energy and coupling strength. The three ways of obtaining a mode energy from the data are the EDC-derived dispersion, the kink energy in the MDC-derived dispersion, and the step in the MDC-derived widths. Theoretically, the mode energy should be the energy to which the peak in the EDC curve decays. However, in cases of weaker mode-coupling behavior, which Fig. 2d is indicative of, the peak intensity decays too fast for this to be an accurate determination in real spectra. On the other hand, in cases of too small a relevant phase space range,

which Fig. 2a is indicative of, the peak intensity does not decay fast enough before another Fermi crossing. If there is a well-defined peak that has enough phase space range in which to decay, the last point at which it can be measured is the best indication of the mode energy. Otherwise, one should resort to the methods described above. The coupling strength is indicated by the extent of the break up of the spectra into a peak and a hump, the washout of the spectra at the mode energy, the sharpness of the "kink" in the MDC-derived dispersion, and the magnitude of the step in the MDC-derived widths. Quantitative assessments of the coupling strength, however, require either a full model calculation or an extraction procedure to invert the phonon density of states coupled to the electronic spectra.

3 Early results on the mode-coupling in the cuprates

Experimental evidence of peak-dip-hump structures was first reported by Dessau et al. and reproduced by Hwu et al. [22, 23]. Shown in Fig. 3 are the first spectra near the $(\pi, 0)$ region in the superconducting state [22]. Due to the relatively poor angular resolution in the earlier experiments, there is substantial momentum integration of the data. The narrow peak emerging in the superconducting state can be attributed to a sharpening of the photoemission peak at low temperatures and a density of states pile-up due to self-de eneone Shownthenga Th hengapTh sharpening. This density of states enhancement is also what causes there to be a singularity d a density

4 Recent results on the mode-coupling in the cuprates

4.1 Half-breathing phonon mode and the spin resonance mode

The introduction of the Scienta analyzer, with its much improved momentum resolution, has changed the landscape of the field. In addition to the peak-dip-hump structures near (π, 0) noted above, a "kink" or abrupt change in the band velocity could be detected in the MDC-derived dispersion along the nodal direction in the zone. This allowed identification of an energy scale without the complications of bi-layer splitting and superstructure inherent in the anti-nodal data discussed above. While there was no controversy over the early data, there remained varying interpretations of the "kinks". Valla et al. did not view the kinks as proof of an energy scale, but rather a smooth curvature in the dispersion in a system near a quantum critical point and therefore with no energy scale [27]. Yet, while the effect may have been weaker than expected for a strongly coupled mode, it was nevertheless present and occurred at an energy of 50 ± 10 meV as shown in Fig. 4, reproduced from Bogdanov et al. [29]. This lead Bogdanov et al. to view the kink as a clear indication of an energy scale in the problem, with a phonon mode, the spin resonance, and the energy gap all possible sources of the renormalization.

Lanzara et al. were the first to positively identify the kink with an oxygen related optical phonon [30]. Figure 5 reproduces the dispersion from several cuprate families along the nodal direction. As shown, the kink is a universal feature and exists in both the normal and superconducting states. Given that this kink occurs at 60–70 meV, these authors attribute the source of the renormalization to the 70 meV in-plane oxygen half-breathing mode seen by neutron scattering [31]. This interpretation explains the data fairly well in the normal state, but is inconsistent with established electron–phonon coupling in the supercon-

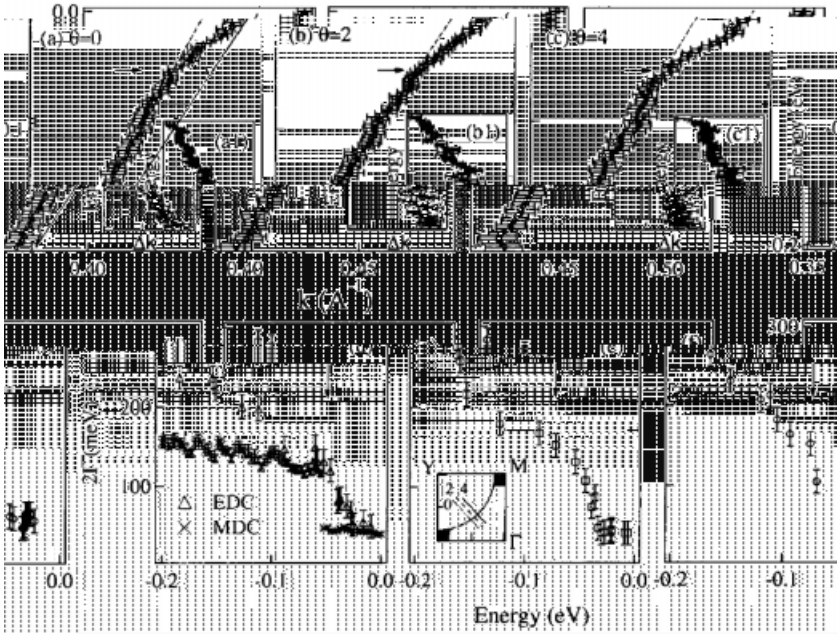

Fig. 4 Panels (a) to (c) show the MDC-derived dispersions (energy vs. momentum) for the underdoped $Bi_2Sr_2CaCu_2O_8$ (T_c = 84 K) for cuts parallel to the Γ–Y direction vs. the momentum. (The positions of the cuts in the BZ are shown in the inset of (e).) The linear fits to the dispersions are also shown. Insets (a1) to (c1) show MDC derived quasiparticle widths in mometnum space along the cuts as a function of binding energy. Panels (e) and (f) show EDC derived quasiparticle widths in energy space along the cuts as a function of binding energy. Panel (d) shows EDC width together with the peak width in energy space derived from MDC of inset (a1) via velocity determined from dispersion of panel (a). Energy is given relative to Fermi energy.

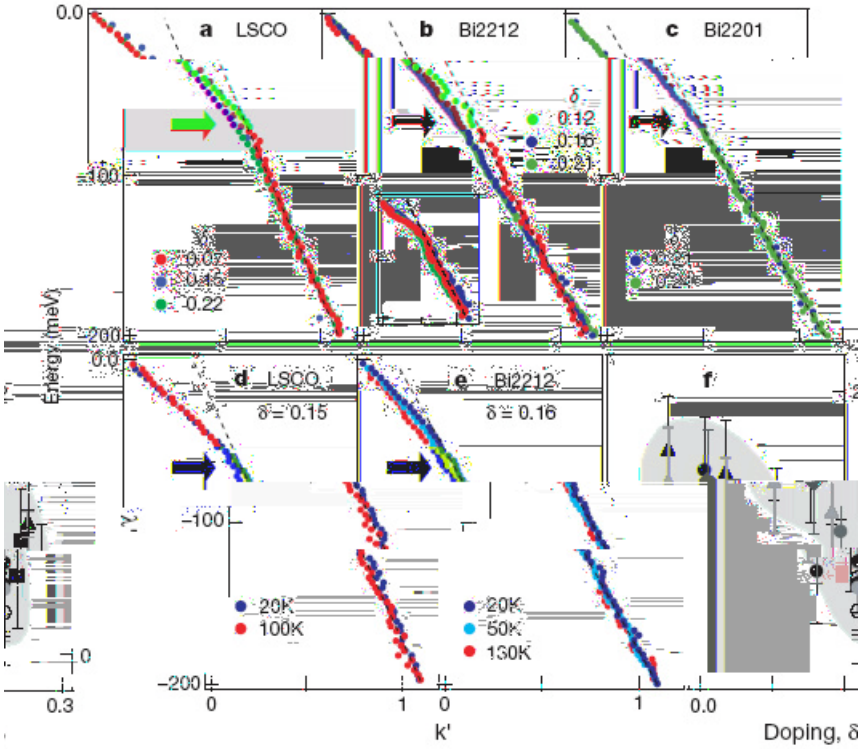

Fig. 5 Ubiquity of a sudden change ('kink') in the dispersion. Top panels are plots of the dispersion (derived from the momentum distribution curves) along (0, 0)–(π, π) (except panel *b* inset, which is off this line) versus the rescaled momentum *k*' for different samples and at different doping levels. (a)–(c) Doping (δ) dependence of the energy dispersion in (a) LSCO (at 20 K), (b) Bi2212 (superconducting state, 20 K), and (c) Bi2201 (normal state, 30 K). Dotted lines are guides to the eye. The kink position is compared with the phonon energy at $q = (\pi, 0)$ (thick red arrow) and the phonon width and dispersion (shaded area) from neutron data [31]. The doping δ was determined from the T_c versus δ universal curve. Inset in (b), dispersions off the (0, 0)–(π, π) direction, showing also a sharpening of the kink on moving away from the nodal direction. The black arrows indicate the position of the kink in the dispersions. (d) and (e) Temperature dependence of the dispersions for (d) LSCO (optimally doped) and (e) Bi2221 (optimally doped). (f) Doping dependence of λ' (see text) along the (0, 0)–(π, π) direction as a function of doping. Data are shown for LSCO (filled triangles) and NdLSCO (1/8 doping; filled diamonds), Bi2201 (filled squares) and Bi2212 (filled circles for the first Brillouin zone, and unfilled circles for the second zone). The different shadings represent data obtained in different experimental runs. Shaded area is a guide to the eye.

ducting state, where the energy at which a mode couples to the electrons should change with the opening of a superconducting gap to the boson frequency plus Δ_0. For optimally doped data, the gap in the anti-nodal region is on the order of 35–40 meV and seemingly does not effect the position at which the electrons couple to the nodal states. Within Migdal–Eliashberg theory, the only way this could happen is if the nodal states did not scatter off the anti-nodal ones at all and therefore were not affected by the singularity in the d-wave density of states. On the other hand, observing a renormalization in the normal state is crucial to any theory. Otherwise, the renormalization seen in the superconducting state could be associated with an effect induced by the superconductivity rather than one that could likely cause it. This issue was later discussed in a broader context of the cuprates [32].

Later on Zhou et al. [33] investigated the doping dependence of LSCO for which the kink can be tracked for a large doping range, and found that the slope of the dispersion near the Fermi level is universal with respect to doping below the kink energy scale or ~70 meV. Above 70 meV, the slope of the

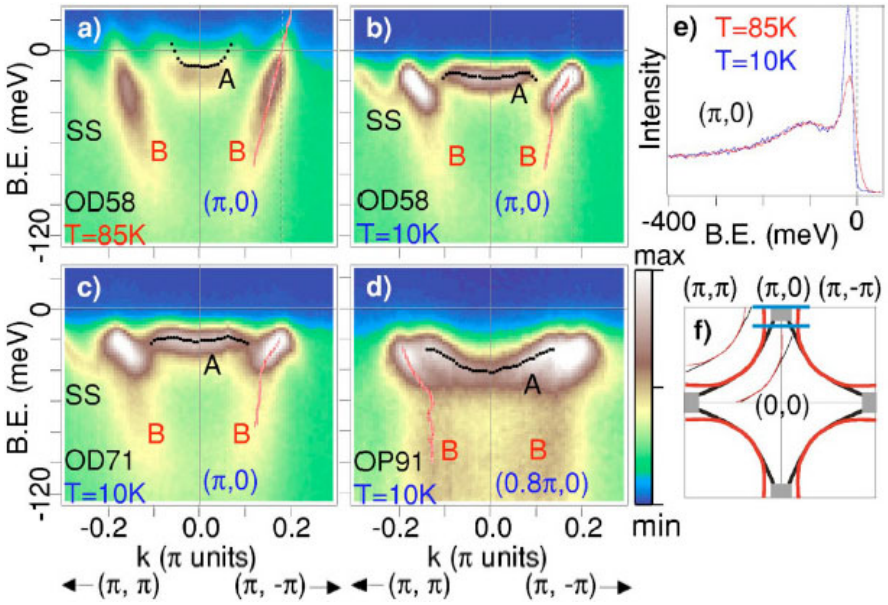

Fig. 6 ARPES dispersion kink near (π, 0). Panel (f) shows the Brillouin zone with bonding band B (red) and antibonding band A (black) Fermi surfaces, as well as cut locations for panels (a)–(d) (blue bars). The B band dispersions (red curves) were determined by fitting MDC peak positions. The black dots represent A band EDC peak positions. Panel (c) shows two representative EDCs at (π, 0) taken from panels (a) and (b).

dispersion becomes significantly steeper towards the under-doped regime, in the opposite direction than one would expect given that the stronger electron–electron interaction nearer to half-filling should naively flatten the electronic bands. These results indicate a potential deviation from the standard Migdal–Eliashberg theory and the possibility of a complex interplay between electron–electron and electron–phonon interactions. Although the doping dependence is still under theoretical investigation, these results represent substantial progress in regard to the behavior of the renormalization along the nodal direction.

In addition to the nodal direction, there was progress made in the anti-nodal region. In particular, Gromko et al. was able to resolve the bonding band well enough in over-doped 58 K and 71 K Bi2212 samples to obtain an MDC-derived dispersion on a single band in the anti-nodal region [34]. Figure 6 reproduces his results. This recent data (see Fig. 6(e)) is representative of the improvement in the quality of ARPES data. The dispersion again exhibits a clear break in the superconducting state (Fig. 6(b), Fig. 6(c), Fig. 6(d)), but seemingly no renormalization in the normal state (Fig. 6(a)). Furthermore the energy scale of this kink was found to be ~40 meV, significantly lower than the nodal kink. Therefore, the renormalization seen in the nodal direction and that seen in the anti-nodal direction appear to be of different origin. The temperature and momentum dependence of the kink in the anti-nodal region led Gromko et al. to interpret the effect as due to the neutron spin resonance, which only appears in the superconducting state. This temperature and momentum dependence identified for a range of doping levels has also led others to attribute the effect to the spin resonance [35, 36]. However, there are some notable inconsistencies with this interpretation: 1) the spin resonance has yet to be observed in such a heavily doped cuprate 2) the oscillator strength of the spin resonance observed by neutron scattering is likely not enough to cause such an effect in ARPES and 3) the Gromko et al. claim of seeing the kink only below T_c bore resemblance to the mode-coupling behavior in Pb tunneling spectra. Namely, electron–phonon coupling in the early tunneling spectra appeared prominently solely in the superconducting state. The linear MDC-derived dispersion in the normal state of Bi2212 at (π, 0) that Gromko et al. reports is not conclusive enough proof that the same mode does not couple to the electrons in the normal state. Nonetheless, the clear determination of mode-coupling in the anti-nodal region, where the gap is maximum,

without the complication of bilayer splitting or superstructure, provides further evidence that the renormalization effects seen by ARPES in the cuprates may indeed be related to the microscopic mechanism of superconductivity.

4.2 The B_{1g} bond-buckling phonon mode

Cuk et al. [8] and Devereaux et al. [9] have recently proposed a new interpretation of the renormalization effects seen in Bi2212. This new interpretation is based primarily on recent data taken at optimal doping, where the renormalization effect is strong throughout the BZ and can be traced in detail from the node to the anti-node; however, the proposal can be naturally extended to the over-doped regime, as well as the superconducting state of the under-doped (pseudo-gap) regime. It explains both the seemingly temperature independent energy scale seen at the node and the 40–50 meV scale seen prominently in the superconducting state of the over-doped sample. Cuk et al. [8] and Devereaux et al. [9] attribute the renormalization seen in the superconducting state to the "bond-buckling" phonon mode involving the out-of-phase motion of the in-plane oxygen. The bond-buckling phonon is observed at 35 meV in the B_{1g} polarization of Raman scattering on an optimally doped sample, the same channel in which the ~35–40 meV d-wave superconducting gap shows up [37–39]. One would then expect the energy position of the mode coupling in the superconducting state to be 70 meV, or the mode energy, 35 meV, plus the maximum gap of 35 meV. Since the gap collapses from 35–40 meV to ~10–15 meV in the over-doped regime, the B_{1g} mode could cause the renormalization both at ~70 meV for optimally doped case as well as at ~40 meV for over-doped case. We note here, however, the energy one would expect for the over-doped renormalization scale is closer to 45–50 meV (35 meV (Ω) + 10 meV (Δ)). However the 40 meV scale quoted by Dessau et al. [34] is most likely a lower bound due to the limited phase space available at $(\pi, 0)$ for identifying an energy scale.

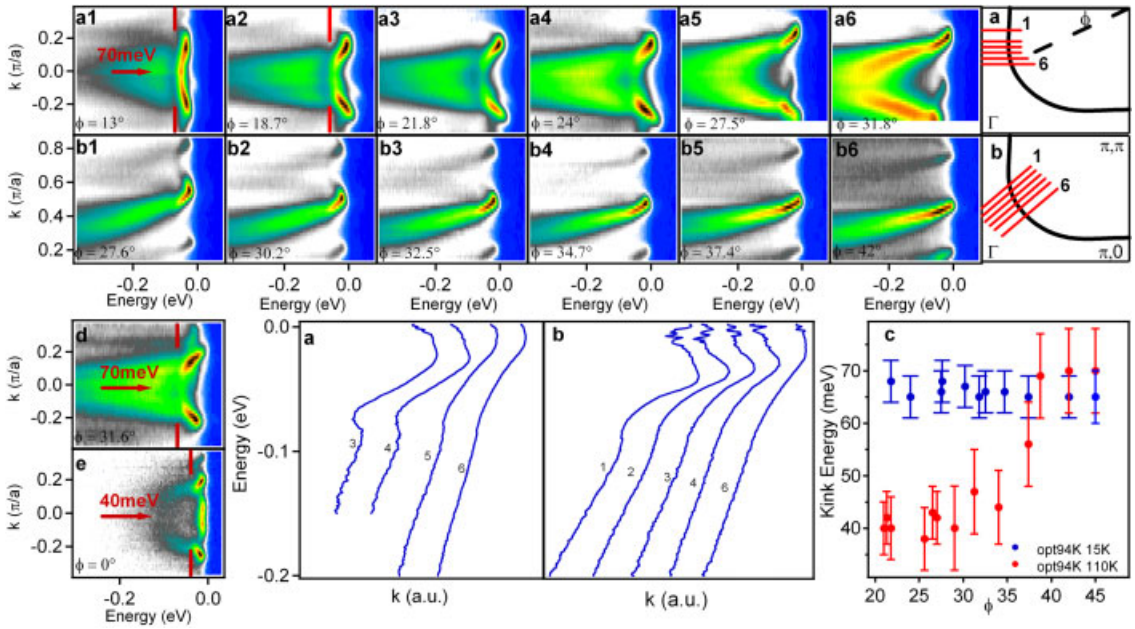

Fig. 7 Image plots in (a1–a6) and (b1–b6) are cuts taken parallel to $(0, \pi)$–(π, π) and $(0, 0)$–(π, π) respectively at the locations indicated in the Brillouin zone ((a) and (b)) at 15 K for an optimally doped sample (T_c = 94 K). MDC-derived dispersions are shown in the panels below the image plots for cuts (a) and (b) respectively. (d) and (e) are spectra taken parallel to $(0, \pi)$–(π, π) at the k-space locations indicated for over-doped (T_c = 65 K) and under-doped samples (T_c = 85 K). (c) summarizes the kink positions in the normal and superconducting states as a function angle in the Brillouin zone.

Given the B_{1g} symmetry, the coupling to the electrons in a tight-binding model of the copper-oxygen plane, is highly anisotropic, and furthermore has a d-wave form factor indicating strong coupling at the anti-node and weak-coupling in the nodal direction. In Fig. 7, we show data from the optimally doped sample for a large portion of the BZ in the superconducting state [8]. The renormalization occurs at 70 meV throughout the BZ and increases in strength from the nodal to anti-nodal points as was noted by others as well [35]. The increase in coupling strength can be seen in the following ways: the s-like shape of the dispersion evident in Fig. 7 (a4), (a5), breaks up into two bands (peak and hump) in Fig. 7 (a2), (a3). Closer to (π, 0), where there is a vHS, the band becomes too narrow to trace a dispersion. The dominant evidence of mode-coupling is a strong depression of spectral weight beyond 70 meV and a minimum in spectral weight at 70 meV (see Fig. 7(a1)). For cuts taken in the (0, 0)–(π, π) direction, the band dispersion is steeper and the effects of mode-coupling, though significant, are less pronounced. Again, the anisotropy of the mode coupling is readily apparent. The s-like shape of the dispersion evident in Fig. 7(b1) closer to (π, 0) evolves into a kink, or simple change in slope of the band, in the nodal direction (Fig. 7(b6)). In addition to resolving the apparent inconsistencies for the 70 meV and 40 meV energy scales, a calculation including the B_{1g} phonon can trace this mode-coupling behavior in detail for an extended momentum space in the zone in the superconducting and normal states.

Tracking the temperature dependence of the 70 meV renormalization in the optimally doped sample, Cuk et al. [8] finds that the kink energy shifts to ~40 meV in the normal state, affirming the assignment to the 35 meV B1g bond-buckling mode. In Fig. 8, Cuk et al. shows the EDC-derived dispersions in the anti-nodal region in the normal and superconducting states with kinks at 40 and 70 meV respectively.

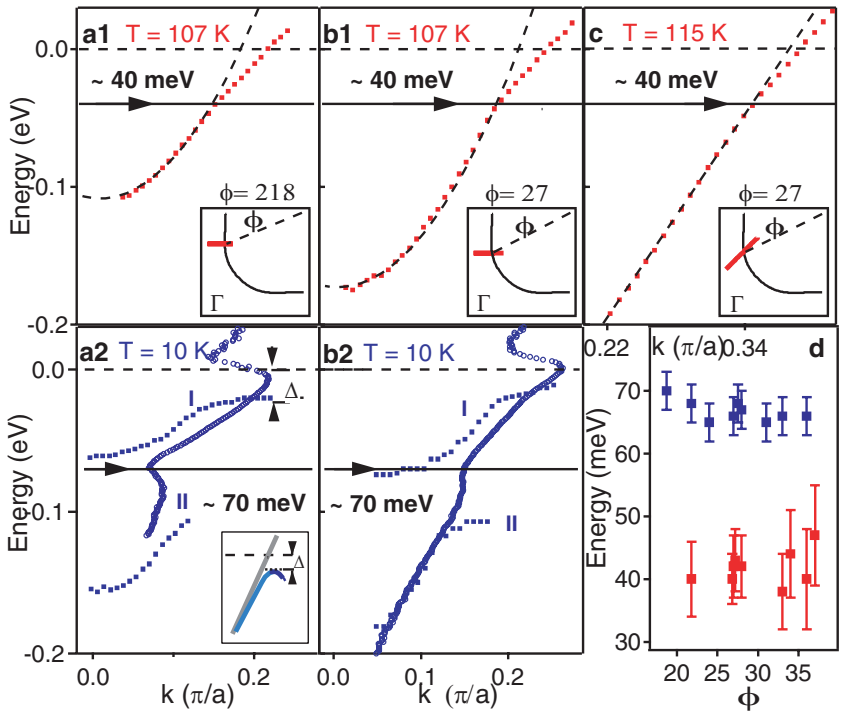

Fig. 8 EDC derived dispersions ((a1), (b1), (c)) in the normal state (107 K and 115 K). ϕ and the cut-direction are noted in the insets. The red dots are the data; the fit to the curve (dashes, black) below the 40 meV line is a guide to the eye. (a2) and (b2) are MDC derived dispersions at the same location and direction as in (a1) and (b1), but in the superconducting state (15 K). In (a2) and (b2) we also plot the peak (I) and hump positions (II) of the EDCs for comparison. The inset of (a2) shows the expected behavior of a Bogoliubov type gap opening. The s-like shape below the gap energy is an artifact of how the MDC handles the back-bend of the Bogoliubov quasiparticle. (d) Kink positions as a function of ϕ in the anti-nodal region.

The effect is considerably weaker in the normal state, confirming the analogy with the case of the strongly-coupled superconductor, Pb. The effect is weak in the normal state for two reasons: 1) the lack of a density of states pile-up as in the superconducting state and 2) the higher temperature, 110 K in the normal state. In Fig. 1(b), we show that the imaginary part of the self energy due to a phonon mode at 110 K is a Fermi function centered at the phonon frequency. Therefore, the onset of the self-energy is broadened by 4.4kT, or 50 meV. The dramatic temperature dependence is captured in the calculations by the difference in the imaginary parts of the self energy shown in Fig 1b and Fig. 1c for the superconducting (10 K) state and the normal (100 K) state respectively. The thermal effect is particularly severe since T_c of the cuprates is high, especially for the Bi-based cuprates. The effect on the spectral function is illustrated more comprehensively in Fig. 12.

By invoking the B_{1g} bond-buckling phonon, then, much of the temperature and momentum dependence of the data can be explained. It cannot, however, explain the observation in the nodal direction of a 70 meV energy scale in the normal state. While the dispersion in Bi2212 data along the nodal direction tends to be washed out and curved in the normal state ($T_c \sim 94$ K), the LSCO data in the normal state ($T_c \sim 10-20$ K) of under-doped samples, shows a clear, well defined kink at 70 meV [25]. The LSCO data is reproduced in Fig. 9. We therefore invoke in the interpretation again the half-breathing mode identified previously as coupling preferentially to the nodal direction. In the data, so far, this mode is seen in the normal state most clearly near the nodal direction and grows weaker as one deviates from the nodal direction of LSCO. In a recent calculation it was shown that the symmetry of the breathing mode combined with the tight-binding band structure gives a coupling strength fairly localized near the node [9].

The full calculation then consists of a tight-binding band structure and el–ph coupling to the breathing mode as well as the B_{1g} bond-buckling mode and is based on an earlier calculation [40]. The electron–phonon coupling vertex $g(k, q)$, where k represents the initial momentum of the electron and q the momentum of the phonon is determined on the basis of the oxygen displacements for each mode in the presence of the underlying band-structure. In the case of the breathing mode, the in-plane displacements of the oxygen modulate the copper–oxygen nearest neighbor hopping integral as well as the site ener-

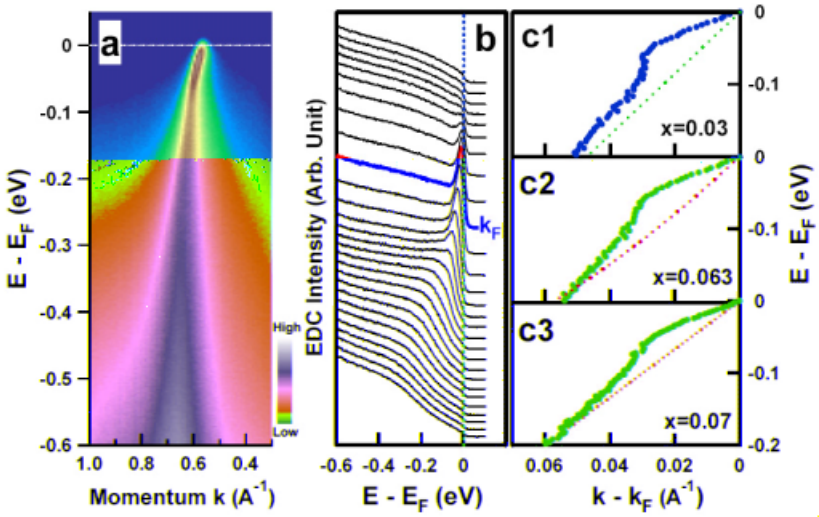

Fig. 9 (a) Typical raw data of two-dimensional image showing the photoelectron intensity as a function of momentum and energy for the LSCO $x = 0.063$ sample. The intensity is expressed as the false-color. The cut was taken along the (0, 0)–(π, π) nodal direction and at a temperature of 20 K. (b) The photoemission spectra (energy distribution curves, EDCs) for the LSCO $x = 0.063$ sample corresponding to (a). The spectrum at the Fermi momentum $k_F = (0.44\pi/a, 0.44\pi/a)$ (red curve) shows a sharp peak. (c) The energy-momentum dispersion for LSCO with (c1) $x = 0.03$, (c2) $x = 0.063$, and (c3) $x = 0.07$ samples, as determined from fitting MDCs.

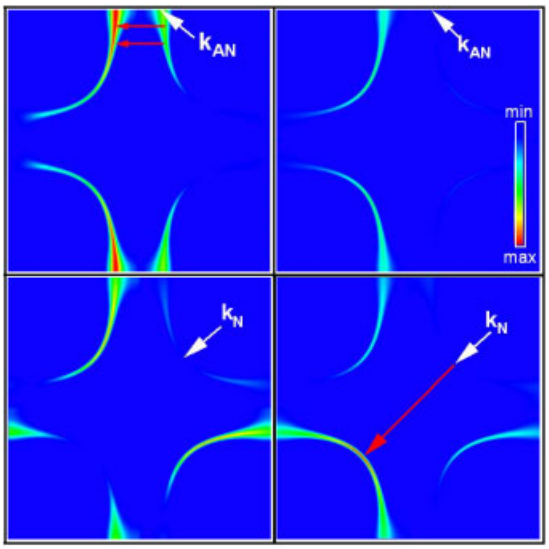

gies. In the case of the bond-buckling mode, one must suppose that the mirror plane symmetry across the copper–oxygen plane is broken in order for electrons to couple linearly to phonons. The mirror plane symmetry can be broken by the presence of a crystal field perpendicular to the plane, tilting of the Cu–O octahedral, static in-plane buckling, or may be dynamically generated.

The $g_{B_{1g}}(k, q)$ form factor leads to preferential $q \sim 2k_f$ scattering between the parallel pieces of Fermi surface in the anti-nodal region, as shown in Fig. 10 depicting $g(k, k')$ for the buckling mode (where $k' = k - q$) for an electron initially at the anti-node (k_{AN}; upper-left) and for an electron initially at the node (k_N; bottom-left). This coupling anisotropy partially accounts for the strong manifestation of electron–phonon coupling in the anti-nodal region where one sees a break up into two bands. The breathing mode, in contrast, modulates the hopping integral and has a form factor, $g_{br}(k, q)$, that leads to preferential scattering for large q and couples opposing nodal states. This coupling anisotropy then accounts for the 70 meV energy scale seen prominently in a narrow k-space region near the nodal direction. Figure 10 also shows that the magnitude of the electron–phonon vertex is largest for an electron initially sitting at the node, k_N, that scatters to the opposing nodal state. For more details on this calculation, see Devereaux et al. [9].

These coupling anisotropies may also be the source of some anomalies in the neutron scattering data on the cuprates. In Fig. 11, we reproduce neutron scattering on YBCO that reveals a softening of the breathing mode with doping for large q ($\sim\pi$) [41] and a softening of the buckling mode through T_c, but only for $q < 2k_f \sim 0.5\pi$ [42]. Again, this indicates that the nodal states are coupled to the ~70 meV half breathing mode while the anti-nodal states are coupled to the ~35 meV bond-buckling mode. However, it is important to note that in the absence of strong electron–electron correlations as is the case of the treatment by Cuk et al. [8] and Devereaux et al. [9], the full breathing mode is more strongly coupled to the electrons than the half-breathing mode. A calculation with electronic correlations shows that the half-breathing mode is more important, and thus is in better agreement with the neutron scattering results [43, 44].

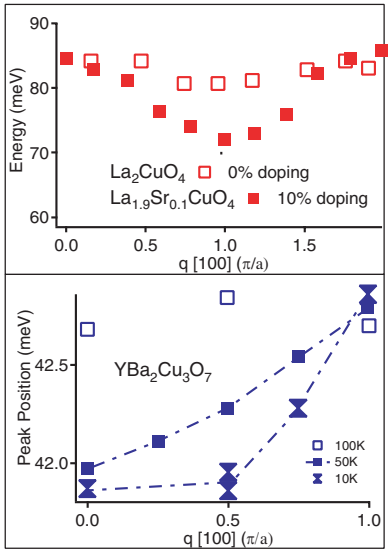

Fig. 11 Upper half of the figure shows neutron scattering data in which the half-breathing mode of La_2CuO_4 softens considerably with doping, but only for large $q(\sim\pi/a)$ [41]. The lower half of the figure shows neutron scattering data in which the B_{1g} "bond-buckling" mode softens with temperature, but only for $q < 0.5\pi/a$ [42].

signatures of electron-phonon coupling seen in the superconducting state at ~70 meV are due to the B_{1g} bond-buckling phonon. The strong anisotropy of the mode-coupling seen in the anti-nodal data between two momentum space cuts separated by only 1/10th of the BZ is captured in the calculation.

The anisotropy of the mode-coupling in both the superconducting state data and the calculation is peculiar to the cuprates. Such a strong anisotropy in the electron–phonon coupling is not traditionally expected. In the cuprates, the sources of the anisotropy are: 1) An electron–phonon vertex for the B_{1g} bond-buckling mode and the breathing mode that depends both on the electron momentum k as well as the phonon momentum q. This comes from a preferential scattering in the Brillouin zone, in which nodal states couple to other nodal states and anti-nodal states to other anti-nodal states. 2) A strongly anisotropic electronic band structure characterized by a van Hove Singularity (vHS) at $(\pi, 0)$. In the anti-nodal region and along the $(\pi, 0)-(\pi, \pi)$ direction in which $2k_f$ scattering is preferred, the bands are narrow, giving rise to a larger electronic density of states near the phonon energy and therefore a stronger manifestation of electron–phonon coupling. 3) A collusion of energy scales in the anti-nodal region that resonate to enhance the above effects – the vHS at ~35 meV in the tight-binding model that best fits the data, the maximum d-wave gap at ~35 meV, and the bond-buckling phonon energy at ~35 meV. All these

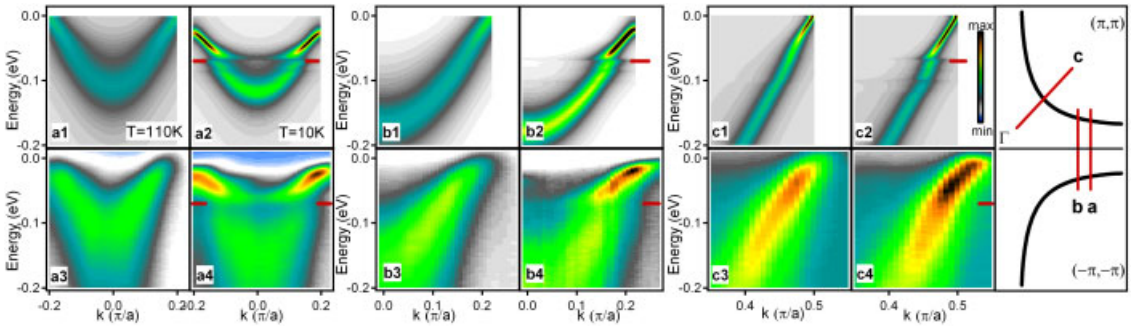

Fig. 12 Image plots of the calculated spectral functions in the normal (a1, b1, c1) and superconducting (a2, b2, c2) states compared to the spectral functions in the normal (a3, b3, c3) and superconducting (a4, b4, c4) states measured in Bi-2212 for momentum cuts *a*, *b*, *c* shown in the right-most panel. The same color scale is used for the normal/superconducting pairs within each cut, but the scaling for the data and the calculation are separate. The red markers indicate 70 meV in the superconducting state.

three factors collide to give the anisotropy of the mode-coupling behavior in the superconducting and normal states. For a detailed look at how each plays a role in the agreement with the data, please see Cuk et al. [45]. The coincidence of energy scales, along with the dominance of the renormalization near the anti-node, indicates the potential importance of the B_{1g} phonon to the pairing mechanism, which is consistent with some theory on the B_{1g} phonon [46–49] but remains to be investigated.

The cuprates provide an excellent platform on which to study the electron–phonon interaction. In one material, such as optimally doped Bi2212, the effective coupling can span λ of order 0.3 at the node to 3 at the anti-node [8, 9]. In addition to the large variation of coupling strength, there is a strong variation in the kinematic considerations for electron–phonon coupling. In the nodal direction, the band bottom is far from the relevant phonon energy scales. However, at the anti-node, the relevant phonon frequencies approach the bandwidth. Indeed the approximation of Migdal, in which higher order vertex corrections to the e1–ph coupling are neglected due to the smallness of $(\lambda \cdot \omega_{\mathrm{ph}}/E_f)$, may be breaking down in the anti-nodal region. Non-adiabatic effect beyond the Migdal approximation have been considered and are under continuing study [50].

4.3 The maximum entropy method

One way to understand the strong signatures of mode coupling seen in the ARPES data is to build a reasonable model based on known experiments and test how well this model agrees with the dominant features seen by ARPES, as shown in Fig. 12. Another way is to de-convolve the signatures of mode coupling from the ARPES data and then compare them with experiments that can directly probe those modes. Both of these methods have been used in the past for obtaining the tunneling spectra in lead, a strong-coupling system – the former approach was used by Scalapino, Schrieffer, and Wilkins [3] and the latter by McMillan and Rowell [4]. In certain special cases, the ARPES signatures of mode-coupling have been de-convolved using the Maximum Entropy Method (MEM). The method is most reliable for determining energy positions of fine features in the data. It is still based on the Eliashberg approach outlined in the introduction and described in more detail above, with the exception that it does not: 1) assume a specific $\alpha^2F(\omega)$ for the phonon density of states coupled to the electrons and 2) assume only one-iteration starting with the free electron and phonon propogators (the MEM procedure iterates until the dispersion data and fit converge). However, the theory implicitly assumes a "Fermi liquid" picture and Migdal's theorem to be valid. In practice, the MEM method has proven to work best in the cuprates along the nodal direction, in the normal state, and at low temperatures. We will discuss these current limitations after presenting data on LSCO, which works best since it can be grown well with low T_c and has strong signatures of mode-coupling along the nodal direction. The MEM method was applied to ARPES data first by Junren et al. on beryllium [51], by extracting $\alpha^2F(\omega)$ from the following form of the Real Self energy:

$$\mathrm{Re}\ \Sigma(\varepsilon, \hat{k}; T) = \int_0^\infty \mathrm{d}\omega\alpha^2F(\omega; \varepsilon, \hat{k})\, K(\varepsilon/kT, \omega/kT)\,, \tag{8}$$

where $K(y, y') = \int_{-\infty}^{\infty} \mathrm{d}x f(x-y)\, 2y'/(x^2 - y'^2)$ with $f(x)$ being the Fermi distribution function.

The MEM method takes this calculated real self energy and finds the best $\alpha^2F(\omega)$ that reproduces the real self energy extracted from the data. The algorithm uses the data to constrain the possibilities that $\alpha^2F(\omega)$ can take. In Fig. 13, we show the extracted $\alpha^2F(\omega)$ for nodal LSCO data, reproduced from Zhou et al. [25]. In addition to the dominant scale ~70 meV scale seen in the dispersion kink, fine features are extracted from the data to give other energy scales. Comparing the extracted $\alpha^2F(\omega)$ to neutron scattering experiments on LSCO one gets a nice agreement of the energy scales to phonon modes as shown in Fig. 13. This result makes it clear that several oxygen related phonon modes are involved with the 70 meV mode being the highest energy mode, a picture consistent with the two mode treatment shown in Fig. 12. It is important to note, however, that this method does not give a good indication of the

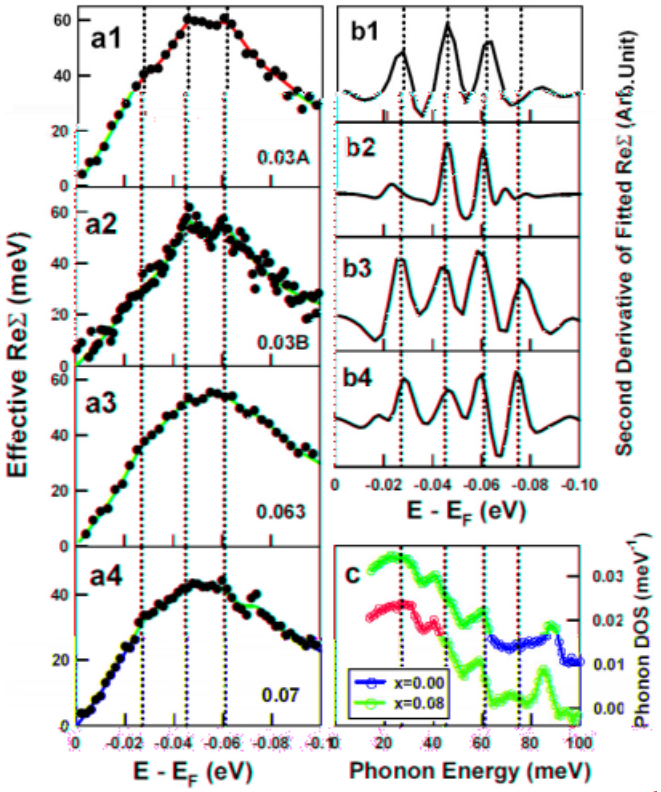

Fig. 13 (a) Effective real part of electron self-energy for LSCO with (a1) $x = 0.03$, (a2) 0.03, (a3) 0.063 and (a4) 0.07. The data in (a2) are obtained on a separate $x = 0.03$ sample using 5 eV pass energy of the electron analyzer in order to take advantage of a smaller energy step (1 meV) while the others are all taken with 10 eV pass energy with a larger energy step. The solid red lines are calculated using the maximum entropy method. (b) The second derivative of the calculated Re Σ. Four dashed line corresponds to energies of 27, 45, 61, and 75 meV. (c) The phonon density of state $F(\omega)$ for LSCO $x = 0$ (red) and $x = 0.08$ (blue) measured from neutron scattering [31, 52]. The four vertical lines correspond to the same energies as in (b).

strength of the electron–phonon coupling. Although the energy positions are well-defined, the intensities for each peak in the extracted $\alpha^2F(\omega)$ vary based on parameters used in the fitting. Nonetheless, the detailed agreement of the energy positions of fine structures in the ARPES data with phonons seen by neutron scattering proves unambiguously that the sharp structures in ARPES data are due to phonon modes.

One would like to extend this method to the superconducting state, in momentum around the BZ, and to higher temperatures. The superconducting state could, in principle, be achieved by using the BCS dispersion of the quasiparticles rather than the normal state dispersion and is currently under study. However, considering the anisotropy of the el–ph coupling for the B_{1g} and half-breathing modes, the anisotropy of the underlying band structure (the vHS), and the d-wave superconducting gap, extending the procedure in momentum may be somewhat more difficult. The $\alpha^2F(\omega, \varepsilon, \hat{k})$ used for the above form of the real self energy is assumed to be only weakly dependent on the initial energy ε and momentum k of the electron. But again, one in principle could begin to consider a different form of the calculated Re Σ and then apply the MEM method with it instead. Extending the method to higher temperatures, for example ~100 K for normal state Bi2212 data, may be, however, a limitation that cannot be overcome. The method's strength is in resolving fine structures due to the phonon density of states. Those fine structures occur predominantly at lower temperatures. At higher temperatures of ~100 K, the imaginary and real parts of the self energy get broadened on the order of the phonon energy itself. In that case, two or more neighboring phonons would contribute to the electronic renormalization at a given energy, both broadening the fine structures in the data and weakening the resolving power of the method itself. So, while the MEM method can directly extract fine features from ARPES data in agreement with neutron scattering without implicitly assuming a phonon model, it does not have the freedom to incorporate the temperature and momentum dependence needed to describe the ARPES data in both superconducting and normal states, near the vHS and near the node. Both modelling of the data and direct extraction, then, are needed, to gain a complete picture of the mode-coupling features in the data.

4.4 Isotope effects in ARPES

Recent experiments by Gweon et al. [53] in which oxygen in Bi2212 samples was isotope exchanged from O(18) to O(16) illuminate the effect that a change in either the electron-phonon coupling constant or phonon frequency has on the ARPES data. This work observed a strongly temperature dependent change in the high energy part of the dispersion that is more pronounced toward the maximum of the d-wave gap [53]. This is a relatively new type of experiment, and further study is warranted. Any evidence of an intrinsically isotope-dependent change in the dispersion, however, would be of considerable use to the phenomenology and theory of the cuprates. The change, however, at higher binding energies is more relevant to multiphonon processes and is not the focus here.

5 Conclusion

ARPES experiments have been instrumental in identifying and detailing the electron-phonon mode coupling behavior in the high-T_c superconductors. The experiments, and related calculations of the spectral function, have shown on the one hand that electron–phonon coupling is crucial for a description of the cuprates, bears resemblence to that seen in established strongly coupled superconductors such as Pb, and may also be important to the microscopic mechanism of superconductivity as in "conventional" superconductors. On the other hand, the experiments and related calculations of the spectral function have also shown that the electron–phonon interaction is strongly anisotropic in momentum and therefore differs from that seen in most other materials. This anisotropy may be in part responsible for obtaining the high T_c's. Other unconventional effects due to a strong "polaronic" electron–phonon interaction and a strong electron–electron interaction, however, must be considered for a full description, but we leave this for an ongoing and later discussion.

References

[1] G. M. Eliashberg, Zh. Eksp. Teor. Fiz. **38**, 966 (1960) [translation: Soviet Phys. – JETP **11**, 696 (1960)].
[2] I. Giaever, H. R. Hart, Jr., and K. Megerle, Phys. Rev. **126**, 941 (1962).
[3] D. J. Scalapino, J. R. Schrieffer, and J. W. Wilkins, Phys. Rev. **148**, 263 (1966).
[4] W. L. McMillan and J. M. Rowell, Phys. Rev. Lett. **14**, 108 (1965).
[5] M. R. Norman et al., Phys. Rev. B **64**, 184508 (2001).
[6] M. L. Kulic, Phys. Rep. **338**, 1 (2003).
[7] A. W. Sandvik, D. J. Scalapino, and N. E. Bickers, Phys. Rev. B **69**, 094523 (2004).
[8] T. Cuk et al., Phys. Rev. Lett. **93**, 117003 (2004).
[9] T. Devereaux et al., Phys. Rev. Lett. **93**, 117004 (2004).
[10] A. S. Mishchenko and N. Nagaosa, Phys. Rev. Lett. **93**, 036402/1-4 (2004).
[11] K. M. Shen et al., xxx.lanl.gov, cond-mat/0407002 (2004).
[12] G. D. Mahan, Many-Particle Physics, 3rd edition (Kluwer Academic/Plenum Publishers, New York, 2000).
[13] A. Damascelli, Z. Hussain, and Z.-X. Shen, Rev. Mod. Phys. **75**, 473 (2003).
[14] C. N. Berglund and W. E. Spicer, Phys. Rev. **136**, A1030 (1964).
[15] A. Damascelli et al., Phys. Rev. Lett. **87**, 239702 (2001).
[16] A. B. Migdal, Zh. Eksp. Teor. Fiz. **34**, 1438 (1958) [translation: Soviet Phys. – JETP **7**, 996 (1958)].
[17] S. Engelsberg and J. R. Schrieffer, Phys. Rev. **131**, 993 (1963).
[18] S. LaShell, E. Jensen, and T. Balasubramanian, Phys. Rev. B **61**, 2371 (2000).
[19] M. Hengsberger et al., Phys. Rev. Lett. **83**, 592 (1999).
[20] T. Valla et al., Phys. Rev. Lett. **83**, 2085 (1999).
[21] S. LaShell, E. Jensen, and T. Balasubramanian, Phys. Rev. B **61**, 2371 (2000).
[22] D. S. Dessau et al., Phys. Rev. Lett. **66**, 2160 (1991).
[23] Y. Hwu et al., Phys. Rev. Lett. **67**, 2573 (1991).
[24] G. B. Arnold, F. M. Mueller, and J. C. Swihart, Phys. Rev. Lett. **67**, 2569 (1991).
[25] X. J. Zhou et al., xxx.lanl.gov, cond-mat/0405130.
[26] M. Eschrig and M. R. Norman, Phys. Rev. Lett. **85**, 3261 (2000).

[27] T. Valla et al., Science **285**, 2110 (1999).
[28] P. W. Anderson, Physica C **341**–**348**, 9 (2000).
[29] P. V. Bogdanov et al., Phys. Rev. Lett. **85**, 2581 (2000).
[30] A. Lanzara et al., Nature **412**, 510 (2001).
[31] R. J. McQueeney et al., Phys. Rev. Lett. **87**, 077001 (2001).
[32] Z. -X. Shen, A. Lanzara, S. Ishihara, and N. Nagaosa, Philos. Mag. B **82**(13), 1349 (2002).
[33] X. J. Zhou et al., Nature **423**, 398 (200349 (2002)..0006r6 w7(Z. -X. Shen, A. Lanzara, S. Ishi)]TJ19/F2 1 Tf15.3082 p.9 NatD. Gromk